

The role of heterointerfaces and subgap energy states on transport mechanisms in silicon heterojunction solar cells

Procel , Paul; Xu , Haiyuan ; Saez, Aurora ; Ruiz Tobon, Carlos; Mazzarella, Luana; Zhao, Yifeng; Han, Can; Yang, Guangtao; Zeman, Miro; Isabella, Olindo

DOI

[10.1002/pip.3300](https://doi.org/10.1002/pip.3300)

Publication date

2020

Document Version

Final published version

Published in

Progress in Photovoltaics: research and applications

Citation (APA)

Procel , P., Xu , H., Saez, A., Ruiz Tobon, C., Mazzarella, L., Zhao, Y., Han, C., Yang, G., Zeman, M., & Isabella, O. (2020). The role of heterointerfaces and subgap energy states on transport mechanisms in silicon heterojunction solar cells. *Progress in Photovoltaics: research and applications*, 28(9), 935-945. <https://doi.org/10.1002/pip.3300>

Important note

To cite this publication, please use the final published version (if applicable).
Please check the document version above.

Copyright

Other than for strictly personal use, it is not permitted to download, forward or distribute the text or part of it, without the consent of the author(s) and/or copyright holder(s), unless the work is under an open content license such as Creative Commons.

Takedown policy




Please contact us and provide details if you believe this document breaches copyrights.
We will remove access to the work immediately and investigate your claim.

RESEARCH ARTICLE



WILEY

The role of heterointerfaces and subgap energy states on transport mechanisms in silicon heterojunction solar cells

Paul Procel  | Haiyuan Xu | Aurora Saez | Carlos Ruiz-Tobon  |
Luana Mazzarella | Yifeng Zhao  | Can Han | Guangtao Yang | Miro Zeman |
Olindo Isabella 

Photovoltaic Materials and Devices Group,
Electrical Sustainable Energy Department,
Delft University of Technology, Delft, The
Netherlands

Correspondence

Paul Procel, Photovoltaic Materials and
Devices Group, Electrical Sustainable Energy
Department, Delft University of Technology,
Mekelweg 4, Delft 2600 AA, The Netherlands.
Email: p.a.procelmoya@tudelft.nl

Funding information

European Union's Horizon 2020 Programme
for Research, Technological Development and
Demonstration, Grant/Award Number:
727523

Abstract

The contact resistivity is a key parameter to reach high conversion efficiency in solar cells, especially in architectures based on the so-called carrier-selective contacts. The importance of contact resistivity relies on the evaluation of the quality of charge collection from the absorber bulk through adjacent electrodes. The electrode usually consists of a stack of layers entailing complex charge transport processes. This is especially the case of silicon heterojunction (SHJ) contacts. Although it is known that in thin-film silicon, the transport is based on subgap energy states, the mechanisms of charge collection in SHJ systems is not fully understood yet. Here, we analyse the physical mechanisms driving the exchange of charge among SHJ layers with the support of rigorous numerical simulations that reasonably replicate experimental results. We observe a connection between recombination and collection of carriers. Simulation results reveal that charge transport depends on the alignment and the nature of energy states at heterointerfaces. Our results demonstrate that transport based on direct energy transitions is more efficient than transport based on subgap energy states. Particularly, for positive charge collection, energy states associated to dangling bonds support the charge exchange more efficiently than tail states. The conditions for optimal carrier collection rely on the Fermi energy of the layers, in terms of activation energy of doped layers and carrier concentration of transparent conductive oxide. We observe that fill factor (FF) above 86% concurrently with 750-mV open circuit voltage can be attained in SHJ solar cells with ρ_c lower than $45 \text{ m}\Omega\cdot\text{cm}^2$ for p-contact and $20 \text{ m}\Omega\cdot\text{cm}^2$ for the n-contact. Furthermore, for achieving optimal contact resistivity, we provide engineering guidelines that are valid for a wide range of silicon materials from amorphous to nanocrystalline layers.

KEYWORDS

charge collection, contact resistivity, interdigitated back contact (IBC), optoelectrical simulations, silicon heterojunction solar cells, trap-assisted tunnelling, tunnelling

1 | INTRODUCTION

Silicon heterojunction (SHJ) solar cells combine crystalline silicon (c-Si) as bulk absorber with thin-film silicon technology as transport stacks for high efficiency based on carrier-selective contacts (CSC). SHJ contact stack typically consists of hydrogenated intrinsic amorphous silicon (i-a-Si:H) layer followed by a doped thin-film silicon^{1–4} (eventually alloyed with oxygen^{5–14} or carbon^{15–17}) and a transparent conductive oxide (TCO). The purpose of these layers is to provide the so-called contact selectivity by inducing an electric potential inside the c-Si for carrier separation that allows the collection of one type of carriers while repelling the other. Brendel and Peibst¹⁸ proposed the quantification of the selectivity by using a parameter that is inversely proportional to recombination parameter (J_0)¹⁹ and contact resistivity (ρ_c). Similarly, the selective transport²⁰ is defined as the ratio of local generation (current) between collecting and no-collecting carriers.²¹ In fact, high selectivity values reflect high quality of CSC and vice versa, requiring both low J_0 and ρ_c values or high current of collecting carriers and minimal current of no-collecting carriers. Accordingly, ρ_c entails the complex electronic transport of carriers, governed by potential barriers and energy discontinuities at interfaces,^{22–25} which are related to the flow of collecting carriers. Additionally, for SHJ contact stack endowed with thin-film silicon layers, ρ_c includes charge transport processes through subgap energy states.^{26–31} Altogether, owing to the complexity of SHJ contact stacks, the driving mechanisms of charge transport in SHJ solar cells are not fully understood, yet. In this respect, rigorous advanced simulation tools can elucidate such physical phenomena.

Besides, Adachi et al.³² demonstrated that reducing carrier recombination also increases the fill factor (FF), thus revealing a link between recombination and resistive losses. This insight anticipated the world-record c-Si conversion efficiency above 26% by combining high passivation quality with low contact resistance.³³ Similarly, research groups reported that in SHJ solar cells, high efficiency depends not only on outstanding passivation but also on low ρ_c ^{34–37}

In particular, Lachenal et al.³⁶ and Lee et al.³⁸ demonstrated remarkable efficiency improvements by minimizing ρ_c . For practical purposes, it is worth noting that among all available techniques for measuring ρ_c , the most straightforward is the transfer length method (TLM).^{25,37} Experimentally,^{1,34–36} it has been proved that minimizing ρ_c of SHJ contact stack system is crucial to reach high efficiency devices. Hence, it is of great interest to investigate the charge transfer mechanisms leading to ρ_c .

In this context, the use of advanced simulations tools is imperative to understand charge transfer mechanisms and their relation to ρ_c and recombination. In this work, based on rigorous TCAD simulations, we present an analysis of the competitive physical mechanisms driving ρ_c for SHJ contact systems. Accordingly, we analyse the transport processes as charge transfer mechanisms supported by not only energy states in conduction or valence band but also subgap states surrounding heterointerfaces. Then, to evaluate the connection between recombination and transport, we deploy and simulate the same SHJ layers in interdigitated back contact (IBC) devices to correlate ρ_c , V_{OC} and FF. Finally, we provide practical insights to reduce ρ_c , thus providing guidelines for improving not only IBC devices but also other solar cell architectures based on SHJ approach. The first results and validation of this investigation were presented in Procel et al.³⁹

2 | CONTACT RESISTIVITY AND TRANSPORT MECHANISMS

To elucidate the intertwined effects of the transport processes, we use contact resistance (ρ_c) as indicator of transport quality. Figure 1A depicts a schematic of TLM measurement structure that consists of two equivalent contacts stack featuring a contact resistance (R_c), separated by a known distance (L). Subsequently, from dark current density–voltage (J - V) curves, calculated for different L , we extract R_c with its equivalent ρ_c as well as the contribution of the semiconductor resistance (R_b) with the equivalent sheet resistance.⁴⁰ In particular, we

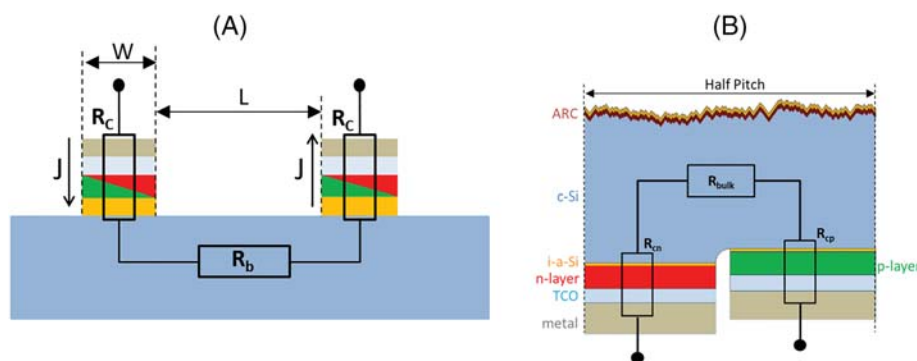


FIGURE 1 (A) Schematic of transfer length method (TLM) structures for contact resistivity (ρ_c) calculation. Contact resistance (R_c) comprises the whole contact stack, from c-Si bulk: i-a-Si (yellow)/doped a-Si (red: n-type, green: p-type)/transparent conductive oxide (TCO) (light blue)/metal (grey) (thicknesses are not in scale). R_c is extracted from current density–voltage (J - V) curves evaluated for different semiconductor resistance (R_b) by changing the contact gap (L). (B) Equivalent lumped resistors indicating resistive losses in interdigitated back contact (IBC) silicon heterojunction (SHJ) devices: contact resistance for n- (R_{cn}) and p-contact (R_{cp}) and bulk resistance (R_{bulk}) [Colour figure can be viewed at wileyonlinelibrary.com]

analyse IBC devices featuring 96% of TCO/metal area coverage to highlight the charge collection through thin-film silicon layers and heterointerfaces up to metal neglecting any effect of the lateral path inside the contact stack.²¹ Therefore, ρ_c allows for calculating the contact resistance contribution in IBC-SHJ devices (see Figure 1B): R_{cn} for n-contact and R_{cp} for the p-contact. For a proper evaluation of ρ_c , the doping type of the base is assumed to have the same doping type of the contact layer stack under analysis,^{37,41} thus avoiding current-blocking effects due to reverse polarization of p-n junction. To assess the transport mechanisms through a TLM structure, we firstly analyse the energy band diagram, as Figure 2 shows. Interestingly, ρ_c is a measurable parameter that describes the local generation of collecting carriers through the complete contact stack, including (i) c-Si carrier accumulation at interfaces with transport stacks (band bending); (ii) potential barrier formed by i-a-Si:H and doped layer, including band offset at c-Si/i-a-Si:H and doped layer/TCO interfaces; and (iii) available energy states in i-a-Si:H, doped layer and TCO. Such a complex contact system exhibits different transport processes for n- and p-contact stack. In this respect, minimal ρ_c maximizes the selective transport²¹ by allowing the maximal flow of collecting carriers through the electrode.

In n-contact case (see Figure 2A), the current flow is based on the movement of electrons across the conduction band. Then, transport through heterointerfaces is based on direct tunnelling (DT) also called field emission,^{42,43} thermionic emission (TE)⁴³ and/or supported with intermediate subgap states in the so-called *trap-assisted tunnelling* (TAT).^{44,45} This mechanism, as it will be explained later, can be either enabled by tail states (TSs) energy states (TAT-TS) or dangling bond energy states (TAT-DBS).

In p-contact case (see Figure 2B), the current flow (J) is based on the movement of positive charges along the valence band of c-Si, i-a-Si:H and p-layer (holes) and TCO conduction band (electrons). In particular, the transport of holes in the valence band is based on DT and TE. At p-layer/TCO interface, the transition from holes to electrons

and vice versa from (to) the valence band of p-layer to (from) conduction band of TCO is based on band-to-band tunnelling (B2BT)⁴⁶ or TAT. B2BT processes are possible with the proper band alignment of valence band of p-layer with conduction band of TCO across equivalent energy states. Such condition is fulfilled if the activation energy (E_a) of p-layer is lower than the energy gap between TCO conduction band and Fermi energy. Besides, subgap energy states also act as carrier reservoir for charge transfer or charge trapping within capture and emission processes (recombination), also known as TAT.^{45,47} Furthermore, the dynamics of capture and emission processes is driven by the Fermi energy relative to defect energy distribution for equivalent capture and emission probability that enables charge transfer mechanisms.^{45,48} Hence, material parameters associated to Fermi-level energy, such as E_a for doped layers and N_{TCO} , ultimately drive the transport of charges through SHJ contact stack.

3 | SIMULATION APPROACH

Figure 1A shows a sketch of the cross section of the simulated TLM structure. On top of a c-Si bulk, two identical contact stacks are localized and spaced by variable gaps (L) (200, 400, 800, 1600 and 2000 μm). Each contact width (W) is 1000 μm , and the stack is formed by 6 nm of i-a-Si:H, 20 nm of doped silicon layer and 140 nm of TCO. Bulk doping is assumed 3 $\Omega\text{-cm}$ for n-type and 8 $\Omega\text{-cm}$ for p-type to calculate ρ_c for n- or p-contact, respectively. The reason for choosing such bulk resistivity stands for the fact that they both exhibit a Fermi level of 250 meV separated from conduction or valence band for n- and p- type, respectively; therefore, the transport conditions inside the absorber bulk are similar for n-contact (electrons) and p-contact (holes). Models and material parameters as well as geometrical parameters for TLM and IBC device are detailed in Tables 1 and 2, respectively. Based on finite element simulator TCAD Sentaurus,⁵⁴ the drift-diffusion equations are numerically solved, consistently including all

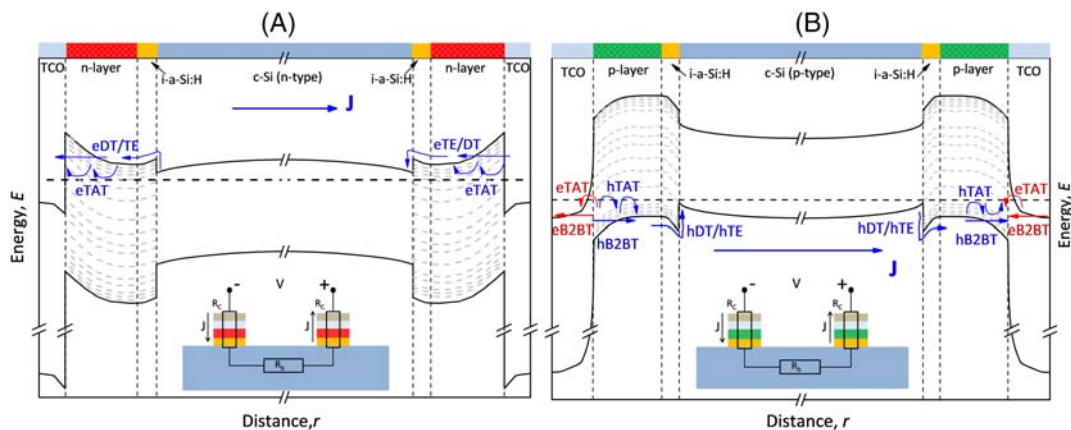


FIGURE 2 Schematic band diagram of transfer length method (TLM) structures for (A) n-contact and (B) p-contact. Transport mechanisms of majority carriers inside c-Si are marked in blue: electrons (e) for n-contact and holes (h) for p-contact. These mechanisms consist of direct tunnelling (DT), thermionic emission (TE) and trap-assisted tunnelling (TAT) through the conduction band or valence band. For p-contact, the charge transport includes also band-to-band tunnelling (B2BT) and TAT at the interface with transparent conductive oxide (TCO) (depicted in red) [Colour figure can be viewed at wileyonlinelibrary.com]

TABLE 1 Summary of models input parameters and material parameters used in simulations

Crystalline silicon				
Model/parameter	Simulated model			
Bandgap narrowing	Schenk ⁴⁹			
Mobility	Klaassen ⁵⁰			
Intrinsic carrier density	Altermatt et al. ⁵¹ $9.65 \times 10^9 \text{ cm}^{-3}$ at 300 K			
Free carrier statistics	Fermi–Dirac			
Intrinsic recombination	Richter et al. ⁵²			
Bulk SRH lifetime	10 ms			
Surface recombination velocity	0.1 cm/s			
Bulk resistivity	5 (n-type)/8 (p-type) $\Omega\cdot\text{cm}$			
SHJ contact materials and properties				
Parameter	i-a-Si:H	n-layer	p-layer	TCO
Electron affinity (eV)	3.9	3.9	3.9	4.9
Band gap (eV)	1.7	1.7	1.7	3.7
Effective CB DOS (cm^{-3})	2×10^{20}	2×10^{20}	2×10^{20}	4×10^{18}
Effective VB DOS (cm^{-3})	2×10^{20}	2×10^{20}	2×10^{20}	1.7×10^{19}
Electron/hole mobility ($\text{cm}^2\text{V}^{-1} \text{ s}^{-1}$)	20/4	25/5	25/5	160/40
Thickness (nm)	6	20	20	140
Activation energy (meV)		Variable	Variable	-
Tunnelling mass (m_0^a)	0.1 (Shannon and Nieuwesteeg ⁵³)	0.1 (Shannon and Nieuwesteeg ⁵³)	0.1 (Shannon and Nieuwesteeg ⁵³)	-
Urbach energy (VB tail) (meV)	50	94	120	-
Urbach energy (CB tail) (meV)	35	68	80	-
Urbach tail pre-factor ($\text{cm}^{-3} \text{ eV}^{-1}$)	1.88×10^{21}	2×10^{21}	2×10^{21}	-
Urbach tail e/h capture cross section (cm^2)	7×10^{-16}	7×10^{-16}	7×10^{-16}	-
Gaussian peak defect density ($\text{cm}^{-3} \text{ eV}^{-1}$)	1.38×10^{16}	1.31×10^{20}	1.31×10^{20}	-
Gaussian donor peak position (eV)	0.89	0.5	1.1	-
Gaussian acceptor peak position (eV)	1.09	0.6	1.2	-
Gaussian donor e/h capture cross section (cm^2)	$3 \times 10^{-14}/3 \times 10^{-15}$	$3 \times 10^{-14}/3 \times 10^{-15}$	$3 \times 10^{-14}/3 \times 10^{-15}$	-
Gaussian acceptor e/h capture cross section (cm^2)	$3 \times 10^{-15}/3 \times 10^{-14}$	$3 \times 10^{-15}/3 \times 10^{-14}$	$3 \times 10^{-15}/3 \times 10^{-14}$	-

^a m_0 is electron rest mass.

the transport processes described in Section 2. J - V curves in dark conditions ($0 < V < 1$ V) are evaluated for different contact spacing to calculate ρ_c , emulating TLM process. In case of no perfectly linear J - V curve, we limit the voltage range to less than 0.15 V, for which the J - V characteristic is sufficiently linear.⁴⁰

To evaluate the contact stack system, we focus our study on material parameters related to Fermi-level energy: E_a for doped layers and TCO carrier concentration (N_{TCO}), assuming N_{TCO} as active dopants. E_a is a measurable parameter describing the energy difference between Fermi level and conduction (valence) band in n-type (p-type) silicon thin-film layers, whereas N_{TCO} establishes the Fermi-energy position relative to the TCO conduction band. Accordingly, low E_a values mean more doping whereas higher N_{TCO} values imply low work

function. Experimentally, low E_a values typically correspond to nanocrystalline silicon material whereas high values correspond to amorphous silicon layers. To adjust E_a in the doped layer, we use a constant doping in addition to energy states distribution as described in Table 1. We consider reasonably attainable values of E_a from 20 up to 350 meV for n-contact and from 30 to 450 meV for p-contact. TCO is modelled on the basis of ITO parameters as degenerate semiconductor⁵⁵ with corresponding values reported in Table 1. Additionally, we include the evaluation of N_{TCO} effect for a range of values from 1×10^{19} up to $1 \times 10^{21} \text{ cm}^{-3}$. It is worth noting that transport processes through heterointerfaces in the electrode stack are almost insensitive to parameters reported in Table 1 as explained in Section 2. Therefore, we assume constant such parameters within our analysis,

TABLE 2 Summary of geometrical parameters for transfer length method (TLM) and interdigitated back contact (IBC) device

Parameter	Value
TLM parameters	
Substrate thickness	250 μm
Contact width	1000 μm
Contact gap	Varied
IBC parameters	
Substrate thickness	100 μm
Pitch	325 μm
p-contact width	200 μm
n-contact width	124 μm

Abbreviations: IBC, interdigitated back contact; TLM, transfer length method.

in order to concisely evaluate the transport mechanisms at contact layers.

Subsequently, to understand the relation of ρ_c with recombination and solar cell external parameters, we performed numerical simulations of IBC structure²¹ (see Figure 1B) using the same contact stack to calculate the external parameters of the solar cell: short circuit current density (J_{sc}), open circuit voltage (V_{oc}), fill factor (FF) and conversion efficiency (η). In order to highlight the main effect of the individual contact under study (n- or p-contact), we assume minimal resistivity contribution from the other contact, by setting the corresponding E_a and N_{TCO} values for minimal ρ_c . Similarly, we consider negligible lateral transport inside bulk, by using relatively small but still realistic 320 μm half pitch. It is worth noting that this approach can be potentially extended to any system of materials based on silicon alloys (e.g., SiO_x or SiC_x) or even using multilayer stacks as reported in Procel et al.²¹ In this work, however, we simulate fully amorphous or nanocrystalline Si layers.

At last, we assume in this work as ohmic the TCO/metal contact in order to emphasize the effect of transport mechanisms explained in Section 2.

4 | RESULTS AND DISCUSSION

As discussed in Section 2, E_a together with N_{TCO} strongly affect the carrier transport and, therefore, ρ_c in SHJ contact stacks. Accordingly, we performed a set of simulations combining doped layers featuring different E_a values with TCO films exhibiting different values of N_{TCO} as described in Section 3. The results of this sensitivity study are graphically explained below in a series of contour plots, elucidating the impact of competitive mechanisms associated to E_a and N_{TCO} on ρ_c , V_{oc} and FF . Then, we analyse FF and V_{oc} to correlate transport and recombination mechanisms to ρ_c . As reported in Procel et al.³⁹ we observe that our simulations accurately reproduce the inner physics of contact stack systems for a wide range of combinations of E_a and N_{TCO} .

4.1 | p-Contact

Figure 3A reports the trend of simulated ρ_c as a function of E_a and N_{TCO} together with experimentally measured ρ_c values of p-type contact stack. Our calculations reasonably replicate experimental results as previously reported in Procel et al.³⁹ The variation of ρ_c values follows different combination of trends, revealing different dominating transport mechanisms depending on E_a and N_{TCO} . To understand the charge transfer processes, we estimated p-layer E_a and N_{TCO} values that concurrently allow the required band alignment for B2BT or either TAT (see Section 2). Accordingly, Figure 3B shows which mechanism, B2BT or TAT, is dominant in the range of parameters investigated.

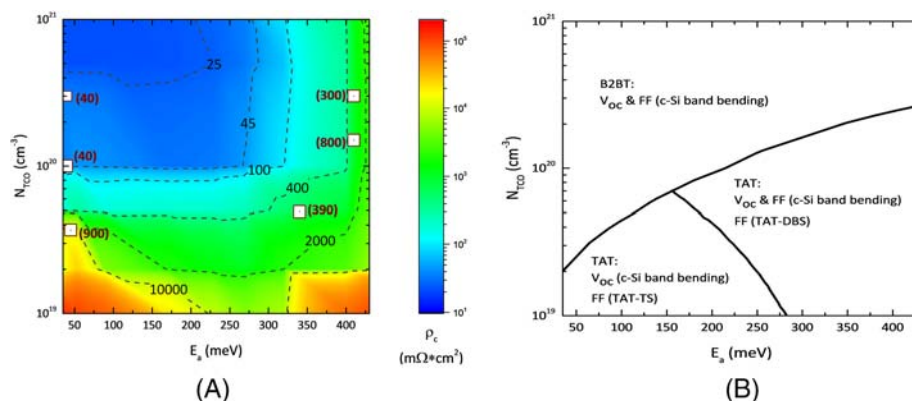


FIGURE 3 (A) Contour plot of ρ_c for p-contact stack as a function of E_a and N_{TCO} . Squared symbols indicate experimentally measured ρ_c .³⁹ (B) Dominating transport process for positive charge collection as a function of E_a and N_{TCO} and their impact on V_{oc} and FF , according to energy alignment of transparent conductive oxide (TCO) conduction band with (i) p-layer valance band (band-to-band tunnelling [B2BT]), (ii) trap-assisted tunnelling (TAT) enabled by tail states energy states (TAT-TS) and (iii) TAT enabled by dangling bond energy states (TAT-DBS). Black lines indicate threshold values of N_{TCO} and E_a for which one transport process takes over another [Colour figure can be viewed at wileyonlinelibrary.com]

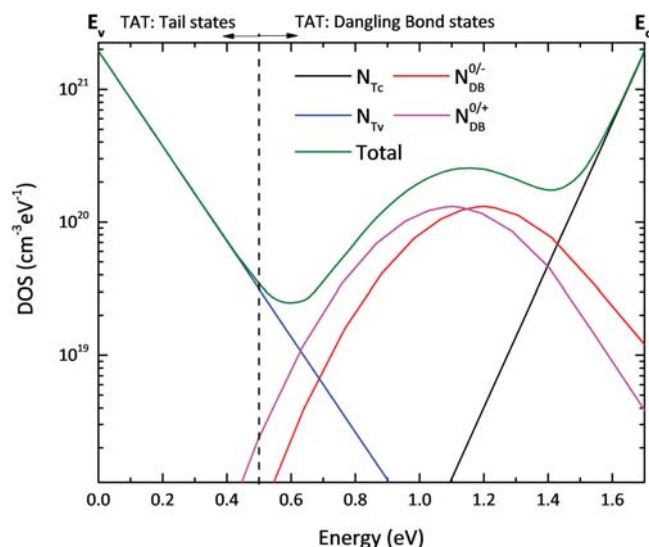


FIGURE 4 Energy states distribution in p-layer (Table 1). N_{TC} , N_{TV} and N_{DB} stand for tail states (TSs) at conduction band (E_C), valence band (E_V) and dangling bonds, respectively. trap-assisted tunnelling (TAT) is enabled by TSs when Fermi energy is lower than 0.5 eV with respect to valence band energy of p-layer at p-layer/transparent conductive oxide (TCO) interface (see Figure 3B). If Fermi energy has a value higher than 0.5 eV with respect to the valence band, then TAT is enabled by dangling bond distribution (DB) [Colour figure can be viewed at wileyonlinelibrary.com]

In case of charge transfer controlled by B2BT processes (see Figure 3B), ρ_c trend is mainly dictated by variation in E_a . N_{TCO} effect is evident for $E_a < 260$ meV revealing a more efficient B2BT by increasing N_{TCO} . In fact, the lowest ρ_c of $22 \text{ m}\Omega\text{-cm}^2$ for p-contact stack corresponds to $E_a = 35$ meV together with $N_{TCO} = 1 \times 10^{21} \text{ cm}^{-3}$. In this scenario, looking at the band diagram in Figure 2B, we can conclude that ρ_c mostly depends on transport mechanisms at c-Si/i-a-Si:H interface, rather than the charge transfer at p-layer/TCO interface, where the B2BT is efficient. It means that c-Si band bending, together with the potential barrier built by i-a-Si:H and doped layer, constrains the charge transport. Interestingly, the conditions for an effective B2BT

(lowest ρ_c values) are twofold: (i) low E_a values that improve c-Si band bending and also lower the potential barrier and (ii) high N_{TCO} values that increase electron accumulation at TCO. The influence of N_{TCO} on ρ_c is stronger for E_a values close to B2BT to TAT threshold. In particular, such influence is significantly evident for low E_a values, evidencing a transition from B2BT to TAT by lowering N_{TCO} values. Note that TLM J - V curves in B2BT regime result in ohmic (linear) contact behaviour.

In case of charge transport based on TAT processes (see Figure 3B), we observe that ρ_c values increase by lowering N_{TCO} . In particular, for $N_{TCO} < 2 \times 10^{19} \text{ cm}^{-3}$, ρ_c exhibits minimal values for $220 < E_a < 320$ meV. This interesting behaviour is explained by looking into the energy of states with similar energy to Fermi energy in Figure 4. As discussed in Section 2, the energy level of subgap states is crucial to define if the state can be charged or discharged in certain conditions.²⁷ Indeed, energy states with equivalent energy to Fermi level exhibit 50% probability to capture or emit a carrier enabling them for charge transport as TAT processes. Therefore, more active states for TAT mechanism are those located close to Fermi energy and surrounding p-layer/TCO interface (Figure 5). In particular, according to our simulations, active energy states are located up to 10 nm from inside p-layer from TCO interface. Figure 4 illustrates the density of states distribution inside the p-layer. In particular, we observe that valence band TSs support TAT mechanisms if the Fermi energy is located within 0.5 eV from the valence band. Similarly, if the Fermi energy is 0.5 eV above the valence band energy, dangling bond states (DBs) support TAT. Figure 3B also shows the combination of E_a and N_{TCO} that enables TAT-based mainly on TS (TAT-TS) or DBS (TAT-DBS). It is worth noting that TAT mainly supported by TAT-TS corresponds to high ρ_c values revealing that TAT-DBS is more effective than TAT-TS for exchange of charge. Such behaviour might be explained by analysing the amphoteric nature of dangling bonds states⁵⁶ compared with the transition processes for valence band TSs. Table 3 summarizes the transition processes for valence band TSs and DBs dominating the charge transfer from p-layer to TCO. These transitions correspond to capture processes exhibiting recombination behaviour as Figure 5 graphically reports.

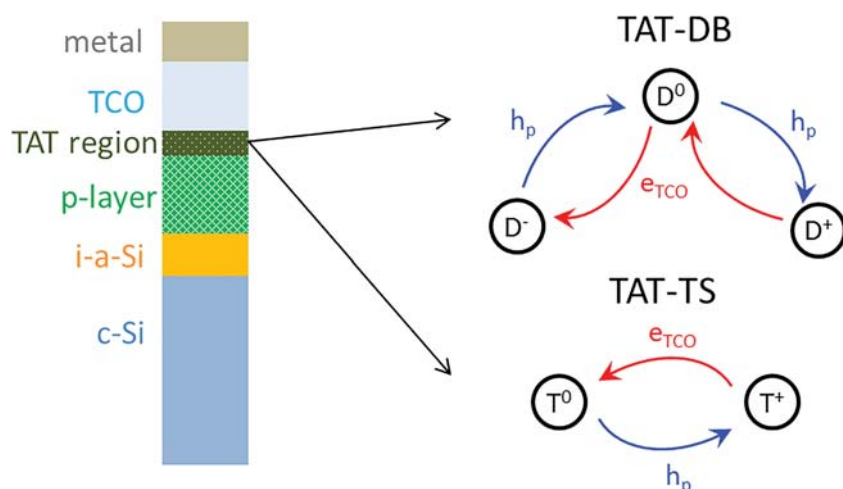


FIGURE 5 Simplified state diagrams for recombination processes on dangling bond (DB) states and tail states (TSs) for collection of positive charge. Trap-assisted tunnelling (TAT) processes occur inside p-layer at p-layer/transparent conductive oxide (TCO) interface (TAT region) [Colour figure can be viewed at wileyonlinelibrary.com]

TABLE 3 Transition processes in valence band tail states (TSs) and dangling bond states (DBSs) for trap-assisted tunnelling (TAT)

Valence band tail states TAT-TS transitions	Dangling bond states TAT-DBS transitions
$T^0 + h_p \rightarrow T^+$	$D^0 + h_p \rightarrow D^+$
$T^+ + e_{\text{TCO}} \rightarrow T^0$	$D^+ + e_{\text{TCO}} \rightarrow D^0$
	$D^0 + e_{\text{TCO}} \rightarrow D^-$
	$D^- + h_p \rightarrow D^0$

Note: For simplicity, T indicates a single-hole state, whereas D indicates a dangling bond state.

For TAT-TS, transition processes are based on single-hole states (T), which are favourable for transport of holes inside p-layer (h_p). However, such states are able to capture an electron from TCO (e_{TCO}) if, and only if, they are positively charged (T^+). It means that a neutral state (T^0) can be only positively charged by an h_p (T^+), allowing thus the capture of e_{TCO} and the apparent transfer of positive charge into TCO. In case of TAT-DBS, transitions from neutral states (D^0) are available for capturing both h_p and e_{TCO} . Accordingly, charged DBSs (D^+ and D^-) promote the transport of charge by capturing whether e_{TCO} or h_p . Indeed, this multistate nature of dangling bonds enhances recombination mechanisms, facilitating the positive charge transport to TCO. Hence, for charge transport between p-layer and TCO, TAT-DBS mechanisms (multistate) are more favourable than TAT-TS (single state) (see Figure 5). This fact is of particular relevance, because it links defect manipulation in thin-film Si layers⁵⁷ to carrier collection improvements. For instance, the enhancement of V_{OC} and FF observed by applying light soaking on SHJ devices.^{58–60} In fact, in TAT regime, transport processes are sensitive to the energy states distribution (nature, energy and density of energy states).

According to Figure 3A,B, TAT-TS dominates charge transport for E_a lower than 250 meV and N_{TCO} below $5 \times 10^{19} \text{ cm}^{-3}$. Here, inefficient TAT-TS hinders the transport of carriers, notwithstanding the

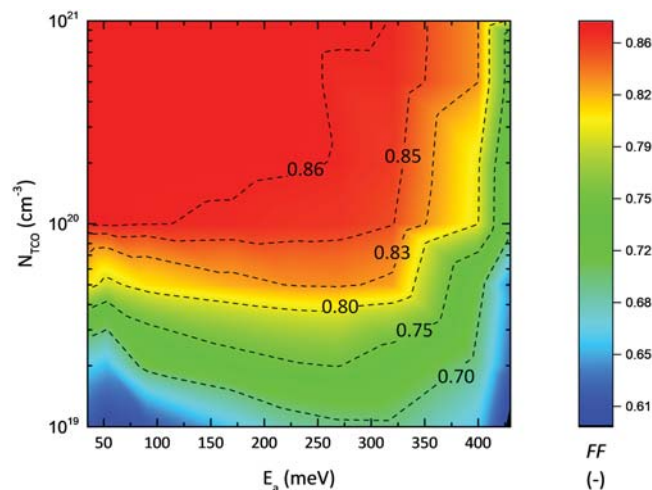


FIGURE 6 FF as a function of E_a and N_{TCO} at p-type stack assuming minimal n-contact resistance³⁹ [Colour figure can be viewed at wileyonlinelibrary.com]

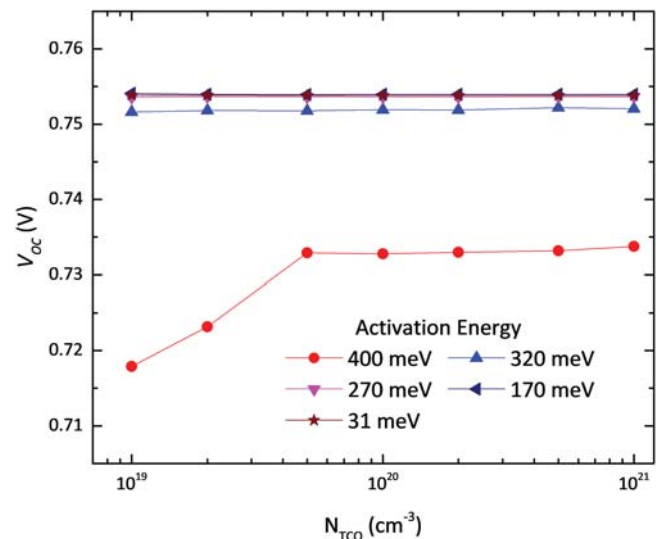


FIGURE 7 V_{OC} as a function of N_{TCO} for different p-layer activation energy (E_a) assuming minimal n-contact resistance [Colour figure can be viewed at wileyonlinelibrary.com]

strong hole accumulation at c-Si/i-a-Si:H interface (c-Si band bending). For low E_a values, increasing N_{TCO} eventually enables B2BT, explaining the sharp ρ_c decrease from 1×10^4 to $400 \Omega\text{-cm}^2$ varying N_{TCO} from 5×10^{19} to $1 \times 10^{20} \text{ cm}^{-3}$. Similarly, increasing E_a expands the space charge region inside p-layer from TCO interface, thus relaxing the alignment of Fermi level with energy states that additionally include dangling bonds with TSs for lower ρ_c values. In case of transport mechanisms dominated by TAT-DBS (see Figure 3B), hole accumulation at c-Si interface (band bending) also plays a role on tunnelling processes (see Section 2), thus explaining ρ_c increase as E_a increases, besides the increase of the potential barrier.²¹ Regarding N_{TCO} , high values relax the energy alignment within dangling bonds for more efficient charge transport based on TAT.

Figure 6 reports simulated FF as a function of E_a and N_{TCO} of IBC-SHJ solar cells. As expected, FF replicates ρ_c trend. In particular, assuming minimal resistive contribution from n-contact and bulk lateral transport, ρ_c values lower than $100 \text{ m}\Omega\text{-cm}^2$ lead to potential FF above 85%. Moreover, correlating Figures 6 and 3B, B2BT mechanisms are associated to $FF > 83\%$. Lowest FF ($FF < 60\%$) values correspond to $N_{\text{TCO}} < 2 \times 10^{19} \text{ cm}^{-3}$ together with $E_a < 170 \text{ meV}$. Interestingly, J - V curves exhibit so-called *s-shape*, resulting from a combination of high ρ_c values with a strong band bending at c-Si/i-a-Si:H interface. In this case, charge transport through p-layer/TCO interface hinders the collection of carriers and therefore lowering FF . The effect of c-Si band bending is apparent by looking at V_{OC} trend in Figure 7. In general, V_{OC} is higher for low E_a values, and it is almost independent of N_{TCO} . In fact, lower E_a values enhance c-Si band bending allowing hole accumulation while repelling electrons and reducing the recombination at c-Si/i-a-Si:H interface. In fact, we observe that V_{OC} is clearly dependent of c-Si band bending as reported in Temmler et al.¹⁶ V_{OC} values remain almost constant ($V_{\text{OC}} \sim 754 \text{ mV}$) for $E_a < 250 \text{ meV}$, when c-Si band bending is larger than 860 meV ,^{21,61,62}

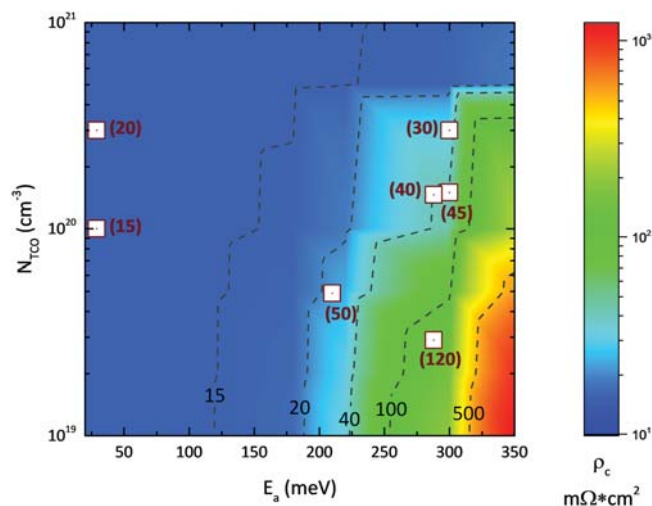


FIGURE 8 ρ_c for n-contact stack as a function of E_a and N_{TCO} . Symbols in the chart indicate experimentally measured ρ_c values (in brackets) taken from Procel et al.³⁹ [Colour figure can be viewed at wileyonlinelibrary.com]

meaning that Fermi level and valence band energy are equivalent close to c-Si/i-a-Si:H interface. However, for $E_a > 380$ meV and $N_{TCO} < 1 \times 10^{19}$ cm⁻³, high ρ_c affects also V_{OC} because subgap energy states act as recombination centres for collecting holes with non-collecting electrons from the absorber bulk rather than electrons from TCO layer. Besides, high V_{OC} calls for low E_a values that are typically associated to nanocrystalline structures. However, high V_{OC} values do not necessarily imply high FF . Indeed, looking at Figures 3B, 6 and 7, high V_{OC} is associated to high FF when charge transport is based on B2BT mechanisms.²¹ Therefore, high-quality transport of positive charge is established by two conditions: (i) strong band bending inside absorber bulk and (ii) band alignment at p-layer/TCO interface for B2BT. Moreover, V_{OC} values depends only on the quality of the c-Si band bending resulting from the electrical potential induced by surrounding layers, whereas FF additionally depends on the quality of charge collection at p-layer/TCO interface. Besides, we highlight that $FF > 80\%$ is possible when transport is supported by TAT-DBS, whereas transport based only on TAT-TS limits FF to values below 80%.

4.2 | n-Contact

As discussed in Section 2, collection of charge through the n-contact implies TAT, TE or DT. Figure 8 shows the trend of simulated ρ_c as a function of E_a and N_{TCO} together with experimentally measured ρ_c values for n-type contact stack. Also in this case, our calculations reasonably replicate experimental results.³⁹ ρ_c exhibits a quite uniform trend in the whole simulation domain with progressively lower values by decreasing E_a and increasing N_{TCO} . In particular, we observe that $\rho_c < 20$ mΩ·cm² corresponds to $E_a < 190$ meV independently of N_{TCO} . Furthermore, we observe generally low ρ_c Figure 8 values with a maximum value of 10^3 mΩ·cm². This value is two order of magnitude

lower than the maximum achieved for p-type contact (see Figure 3A). Here, the charge transfer through n-contact stack occurs only in the conduction band (see Figure 2). Low E_a values are favourable for charge transport because they (i) enhance the conduction band bending inside c-Si improving carrier states at c-Si/(i)-a-Si:H interface and (ii) lower the potential barrier, increasing the tunnelling probability for whatever TAT, TE or DT. Note that in this case, it is not possible to differentiate each individual contribution, because all mechanisms exhibit similar effects on transport owing to the proven band alignment between conduction bands. High N_{TCO} values entail a reduction of TCO work function, which positively affects the collection of electrons.⁶³ Looking at the cell results in Figures 9 and 10, FF and V_{OC} follow similar trends. V_{OC} and FF are almost insensitive to N_{TCO} for E_a lower than 230 meV. For E_a values higher than 230 meV, FF and V_{OC} exhibit an increase trend by rising N_{TCO} . This is ascribed to the positive influence of TCO work function effect that becomes apparent by lowering the potential barrier size.²¹ Interestingly, for $\rho_c < 20$ mΩ·cm² ($E_a < 190$ meV), both V_{OC} and FF reach a plateau. We calculate optimal $V_{OC} = 754$ mV and $FF = 86.6\%$ for the minimal $\rho_c = 15$ mΩ·cm² ($E_a = 20$ meV, $N_{TCO} = 1 \times 10^{21}$ cm⁻³). We observe that the minimal ρ_c for n-contact is lower than minimal ρ_c for p-contact by 8 mΩ·cm². Such a difference is ascribed to inherent c-Si/i-a-Si:H band offset, that is, around 400 meV larger for hole transport than electron transport. Moreover, if transport is based on DT, B2BT or TE, c-Si band bending at c-Si/i-a-Si:H interface affects the quality of tunnelling processes, thus lowering ρ_c values. It means that a strong c-Si band bending reduces ρ_c and vice versa. The band bending inside c-Si also depends on Fermi-level energy with respect to conduction or valence band in the quasineutral region. Accordingly, by changing wafer resistivity (changing Fermi-level position in c-Si bulk) also affects the band bending, which eventually impacts on ρ_c calculations as reported on Lachenal et al.³⁶

Regarding ultimate IBC conversion efficiency, as expected, minimal ρ_c values for n- and p-contact result in the calculated maximal

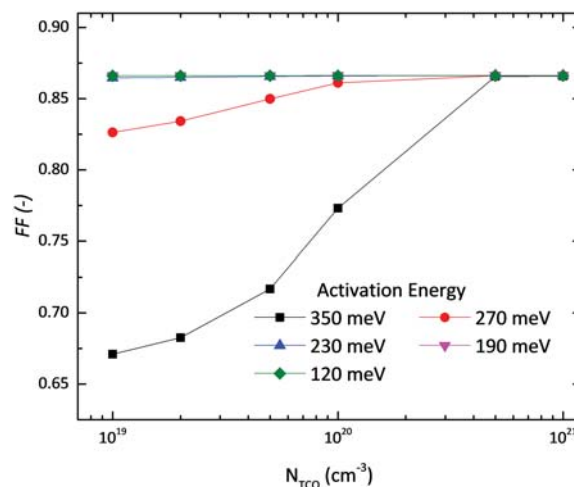


FIGURE 9 FF as a function of N_{TCO} at for different n-layer activation energy (E_a), assuming minimal p-contact resistance [Colour figure can be viewed at wileyonlinelibrary.com]

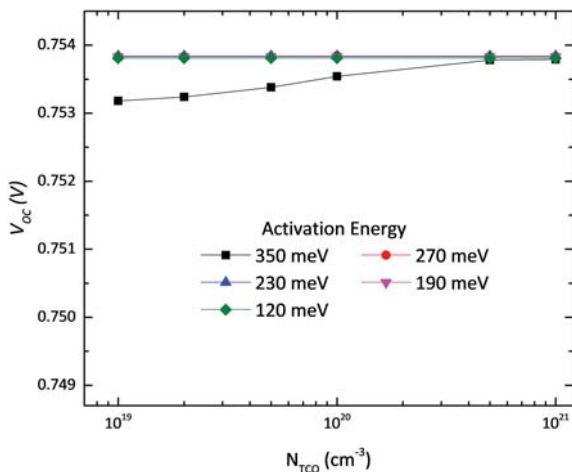


FIGURE 10 V_{OC} as a function of N_{TCO} at for different n-layer activation energy (E_a), assuming minimal p-contact resistance [Colour figure can be viewed at [wileyonlinelibrary.com](https://onlinelibrary.wiley.com)]

$FF = 86.6\%$ and $V_{\text{OC}} = 754 \text{ mV}$ that also brings η well above 26% depending on light management techniques yielding $J_{\text{SC}} > 40 \text{ mA/cm}^2$. Concerning J_{SC} , we observed a variation of less than 0.04 mA/cm^2 due to transport processes. In this respect, J_{SC} depends mostly on light management approach rather than transport mechanisms.

Hence, optimizing ρ_c highlights the path for enhancing IBC conversion efficiency. It is worth noting that also other SHJ architectures can be evaluated, but considering more specialized analysis focussed on front contact layers, that additionally include lateral transport inside and surrounding the front contact stack.

5 | CONCLUSIONS

We have analysed the physical mechanisms driving the charge exchange in SHJ contact systems by advanced electrical modelling of TLM contact stacks. We studied the dominating mechanisms that govern contact resistivity (ρ_c) for both p- and n-type contact stacks by varying activation energy (E_a) in doped layer and doping concentration in TCO (N_{TCO}). The energy alignment and potential barriers at heterointerfaces drive the transport of carriers in terms of tunnelling processes (DT, B2BT or TAT) or TE. Therefore, E_a and N_{TCO} are relevant parameters as they are related to the Fermi energy and thus to the alignment of energy states (including subgap states). Our calculations are consistent with experimentally retrieved ρ_c values, thus our simulations accurately describe the physical phenomena occurring at heterointerfaces and thin-film layers. The simulation results show that for the n-contact, the transport processes imply alignment of energy states within the conduction band in terms of DT, TAT or TE. In case of p-contact, charge transfer processes are more complex and additionally include B2BT supported also by TAT mechanisms.

For p-contact, our model reveals peculiar ρ_c trends marked by B2BT or TAT mechanisms. In general, transport based on direct energy transitions (B2BT) is more efficient than transport based on

transition to subgap energy states (TAT). In particular, among TAT processes, TAT based on dangling bonds (TAT-DBS) are more efficient for charge transport than those based on TSs (TAT-TS). This is because of the amphoteric nature of dangling bonds, which allows more recombination states. Thus, a neutral DBS enables the transport of a hole from the absorber bulk or an electron from TCO, whereas a neutral TS only enables the transport of a hole. If B2BT is dominant, then ρ_c exhibits a clear dependence on E_a rather than N_{TCO} , since ρ_c decreases for low E_a values. When TAT controls the transport of carriers, ρ_c depends more on N_{TCO} than E_a . In this case, increasing N_{TCO} results in the reduction of ρ_c by relaxing the energy alignment inside the p-layer up to 10 nm, including DBSs at p-layer/TCO interface. Accordingly, more efficient transport of charge could be achieved by increasing DBSs inside the p-layer by annealing, light soaking or bias voltage. Regarding the external parameters of IBC-SHJ solar cell, when B2BT processes dominate the transport of carriers, simulated V_{OC} , FF exhibit similar trend to ρ_c owing to induced band bending inside c-Si absorber bulk. In case of TAT regime, FF and ρ_c depend on the alignment of aforementioned dangling bonds or TSs at p-layer/TCO interface whereas V_{OC} is almost insensitive to N_{TCO} . Regarding n-contact, our calculations show that ρ_c is more determined by E_a than N_{TCO} . In general, decreasing E_a while increasing N_{TCO} results on minimal ρ_c values. By comparing ρ_c in p- and n-contact, for p-contact, ρ_c changes about five orders of magnitude by varying E_a and N_{TCO} whereas n-contact ρ_c varies only two orders of magnitude. Such a difference reveals that p-contact is more sensitive to layer properties and therefore requires more effort to be optimized. As guideline for optimal contact stack design, we calculated the minimal ρ_c of 22 and 15 $\text{m}\Omega\cdot\text{cm}^2$ for p- and n-contact, respectively, corresponding to $E_a < 30 \text{ meV}$ and $N_{\text{TCO}} > 5 \times 10^{20} \text{ cm}^{-3}$. For such minimal ρ_c values, we calculated 754 mV and 86.6% as the ultimate V_{OC} and FF , respectively. These values can be concurrently achieved and, depending on light management techniques applied, allow to obtain the highest possible conversion efficiency in IBC-SHJ solar cells. Hence, the optimization of ρ_c is practically crucial to achieve high efficiency not only in IBC-SHJ solar cells but also in other architectures. However, the optimization of other SHJ solar cells demands more specialized analysis, focussing on front contact layers that additionally includes lateral transport inside and surrounding the front contact stack.

ACKNOWLEDGEMENTS

This work has been performed in the framework of NextBase project, that has received funding from the European Union's Horizon 2020 Programme for Research, Technological Development and Demonstration under Grant agreement no. 727523. The authors acknowledge the NextBase project consortium for fruitful discussions.

ORCID

Paul Procel  <https://orcid.org/0000-0003-4997-3551>

Carlos Ruiz-Tobon  <https://orcid.org/0000-0002-3184-4543>

Yifeng Zhao  <https://orcid.org/0000-0003-3789-5090>

Olindo Isabella  <https://orcid.org/0000-0001-7673-0163>

REFERENCES

- Nogay G, Seif JP, Riesen Y, et al. Nanocrystalline silicon carrier collectors for silicon Heterojunction solar cells and impact on low-temperature device characteristics. *IEEE J Photovoltaics*. Nov. 2016;6(6):1654-1662.
- Seif JP, Descoedres A, Nogay G, et al. Strategies for doped nanocrystalline silicon integration in silicon heterojunction solar cells. *IEEE J Photovoltaics*. 2016;6(5):1132-1140.
- Battaglia C, Cuevas A, De Wolf S. High-efficiency crystalline silicon solar cells: status and perspectives. *Energ Environ Sci*. 2016;9(5):1552-1576.
- Allen TG, Bullock J, Yang X, Javey A, De Wolf S. Passivating contacts for crystalline silicon solar cells. *Nat Energy*. Sep. 2019;4(11):914-928.
- Mazzarella L, Morales-Vilches AB, Korte L, Schlattmann R, Stannowski B. Ultra-thin nanocrystalline n-type silicon oxide front contact layers for rear-emitter silicon heterojunction solar cells. *Sol Energy Mater Sol Cells*. 2018;179(November 2017):386-391.
- Mazzarella L, Kirner S, Gabriel O, et al. Nanocrystalline silicon emitter optimization for Si-HJ solar cells: substrate selectivity and CO₂ plasma treatment effect. *Phys Status Solidi*. 2017;214(2):1532958. <https://doi.org/10.1002/pssa.201532958>
- Mazzarella L, Morales-Vilches AB, Hendrichs M, et al. Nanocrystalline n-type silicon oxide front contacts for silicon heterojunction solar cells: photocurrent enhancement on planar and textured substrates. *IEEE J Photovoltaics*. 2017;8(1):70-78.
- Kirner S, Mazzarella L, Korte L, Stannowski B, Rech B, Schlattmann R. Silicon heterojunction solar cells with nanocrystalline silicon oxide emitter: insights into charge carrier transport. *IEEE J Photovoltaics*. 2015;5(6):1601-1605.
- Park H, Lee Y, Park SJ, et al. Tunnel oxide passivating electron contacts for high-efficiency n-type silicon solar cells with amorphous silicon passivating hole contacts. *Prog Photovoltaics Res Appl*. Oct. 2019;27(12):1104-1114.
- Richter A, Smirnov V, Lambert A, Nomoto K, Welter K, Ding K. Versatility of doped nanocrystalline silicon oxide for applications in silicon thin-film and heterojunction solar cells. *Sol Energy Mater Sol Cells*. Jan. 2018;174:196-201.
- Ding K, Aeberhard U, Finger F, Rau U. Silicon heterojunction solar cell with amorphous silicon oxide buffer and microcrystalline silicon oxide contact layers. *Phys Status Solidi Rapid Res Lett*. 2012;6(5):193-195.
- Peter Seif J, Descoedres A, Filipič M, et al. Amorphous silicon oxide window layers for high-efficiency silicon heterojunction solar cells. *J Appl Phys*. 2014;115(2):024502. <https://doi.org/10.1063/1.4861404>
- Nakada K, Irikawa J, Miyajima S, Konagai M. Silicon heterojunction solar cells with high surface passivation quality realized using amorphous silicon oxide films with epitaxial phase. *Jpn J Appl Phys*. May 2015;54(5):052303. <https://doi.org/10.7567/JJAP.54.052303>
- Zhao Y, Mazzarella L, Procel P, et al. Doped hydrogenated nanocrystalline silicon oxide layers for high-efficiency c-Si heterojunction solar cells. *Progress in Photovoltaics: Research and Applications*. 2020;28(5):425-435. <https://doi.org/10.1002/pip.3256>
- van Cleef MWM, Rubinelli FA, Rizzoli R, Pighini R, Schropp REI, van der Weg WF. Amorphous silicon carbide/crystalline silicon heterojunction solar cells: a comprehensive study of the photocarrier collection. *Jpn J Appl Phys*. Jul. 1998;37, no. Part 1, No. 7A: 3926-3932.
- Temmler J, Bivour M, Steinkemper H, Hermle M. "Boron doped A-Si: H front Layers for silicon heterojunction cells," 2014, pp. 481-483.
- Zhang D, Deligiannis D, Papakonstantinou G, van Swaaij RACMM, Zeman M. Optical enhancement of silicon Heterojunction solar cells with hydrogenated amorphous silicon carbide emitter. *IEEE J Photovoltaics*. Nov. 2014;4(6):1326-1330.
- Brendel R, Peibst R. Contact selectivity and efficiency in crystalline silicon photovoltaics. *IEEE J Photovoltaics*. 2016;6(6):1-8.
- Cuevas A. The recombination parameter J₀. *Energy Procedia*. 2014; 55:53-62.
- Wurfel U, Cuevas A, Wurfel P. Charge carrier separation in solar cells. *IEEE J Photovoltaics*. 2015;5(1):461-469.
- Procel P, Yang G, Isabella O, Zeman M. Theoretical evaluation of contact stack for high efficiency IBC-SHJ solar cells. *Sol Energy Mater Sol Cells*. Nov. 2018;186(June):66-77.
- Chang CY, Fang YK, Sze SM. Specific contact resistance of metal-semiconductor barriers. *Solid State Electron*. Jul. 1971;14(7):541-550.
- Yu AYC. Electron tunneling and contact resistance of metal-silicon contact barriers. *Solid State Electron*. Feb. 1970;13(2):239-247.
- Roy AM, Lin JYJ, Saraswat KC. Specific contact resistivity of tunnel barrier contacts used for Fermi level depinning. *IEEE Electron Device Lett*. Oct. 2010;31(10):1077-1079.
- Schroder DK, Meier DL. Solar cell contact resistance—a review. *IEEE Trans Electron Devices*. May 1984;31(5):637-647.
- Furlan J, Gorup Z, Smole F. Modeling tunneling-assisted generation-recombination rate in space-charge region of Pn a-Si:H junction. *J Model Simul Microsystems*. 1999;1(2):109-114.
- Smole F, Furlan J. Effects of abrupt and graded a-Si:C:H/a-Si:H interface on internal properties and external characteristics of p-i-n a-Si:H solar cells. *J Appl Phys*. Dec. 1992;72(12):5964-5969.
- Arch JK, Rubinelli FA, Hou J-Y, Fonash SJ. Computer analysis of the role of p-layer quality, thickness, transport mechanisms, and contact barrier height in the performance of hydrogenated amorphous silicon p-i-n solar cells. *J Appl Phys*. May 1991;69(10):7057-7066.
- Hack M, Shur M. Theoretical modeling of amorphous silicon-based alloy p-i-n solar cells. *J Appl Phys*. 1983;54(10):5858. <https://doi.org/10.1063/1.331812>
- Zeman M, Krc J. Electrical and optical modelling of thin-film silicon solar cells. *MRS Proc*. Jan. 2007;989:0989-A03-01. <https://doi.org/10.1557/PROC-0989-A03-01>
- Zeman M, Willemen JA, Vosteen LLA, Tao G, Metselaar JW. Computer modelling of current matching in a-Si:H/a-Si:H tandem solar cells on textured TCO substrates. *Sol Energy Mater Sol Cells*. May 1997;46(2):81-99.
- Adachi D, Hernández JL, Yamamoto K. Impact of carrier recombination on fill factor for large area heterojunction crystalline silicon solar cell with 25.1% efficiency. *Appl Phys Lett*. Dec. 2015;107(23):233506. <https://doi.org/10.1063/1.4937224>
- Yoshikawa K, Kawasaki H, Yoshida W, et al. Silicon heterojunction solar cell with interdigitated back contacts for a photoconversion efficiency over 26%. *Nat Energy*. Mar. 2017;2(3):17032. <https://doi.org/10.1038/nenergy.2017.32>
- Nogay G, Stuckelberger J, Wyss P, et al. Silicon-rich silicon carbide hole-selective rear contacts for crystalline-silicon-based solar cells. *ACS Appl Mater Interfaces*, p. acsami.6b12714. 2016;8(51):35660-35667.
- Bullock J, Hettick M, Geissbühler J, et al. Efficient silicon solar cells with dopant-free asymmetric heterocontacts. *Nat Energy*. Jan. 2016;1(3):15031. <https://doi.org/10.1038/nenergy.2015.31>
- Lachenal D, Papet P, Legradic B, et al. Optimization of tunnel-junction IBC solar cells based on a series resistance model. *Sol Energy Mater Sol Cells*. Sep. 2019;200(March):110036. <https://doi.org/10.1016/j.solmat.2019.110036>
- Lachenal D, Baetzner D, Frammelsberger W, et al. Heterojunction and passivated contacts: a simple method to extract both n/tco and p/tco contacts resistivity. *Energy Procedia*. 2016;92:932-938.
- Lee S-Y, Choi H, Li H, et al. Analysis of a-Si:H/TCO contact resistance for the Si heterojunction back-contact solar cell. *Sol Energy Mater Sol Cells*. Jan. 2014;120(PART A):412-416.
- Procel P, et al. "On the correlation between contact resistivity and high efficiency (IBC-) SHJ solar cells," in Proceedings of the 36th European Photovoltaic Solar Energy Conference and Exhibition, 2019, pp. 255-258.

40. Schade H, Smith ZE. Contact resistance measurements for hydrogenated amorphous silicon solar cell structures. *J Appl Phys.* 1986;59(5):1682-1687.
41. Rienacker M, Bossmeyer M, Merkle A, et al. Junction resistivity of carrier-selective Polysilicon on oxide junctions and its impact on solar cell performance. *IEEE J Photovoltaics.* Jan. 2017;7(1):11-18.
42. Sze SM, Ng KK. *Physics of Semiconductor Devices.* 3rd ed. Hoboken, NJ, USA: John Wiley & Sons, Inc.; 2006.
43. MeiKei I, Solomon PM, Laux SE, Wong HSP, Chidambarao D. "Comparison of raised and Schottky source/drain MOSFETs using a novel tunneling contact model," Int. Electron Devices Meet. 1998. Tech. Dig. (Cat. No.98CH36217), pp. 733-736, 1998.
44. Jiménez-Molinos F, Gámiz F, Palma A, Cartujo P, López-Villanueva JA. Direct and trap-assisted elastic tunneling through ultrathin gate oxides. *J Appl Phys.* 2002;91(8):5116-5124.
45. Goes W, Wimmer Y, el-Sayed AM, et al. Identification of oxide defects in semiconductor devices: a systematic approach linking DFT to rate equations and experimental evidence. *Microelectron Reliab.* Aug. 2018;87(April):286-320.
46. Kane EO. Theory of tunneling. *J Appl Phys.* 1961;32(1):83-91.
47. Palma A, Godoy A, Jiménez-Tejada J, Carceller J, López-Villanueva J. Quantum two-dimensional calculation of time constants of random telegraph signals in metal-oxide-semiconductor structures. *Phys Rev B - Condens Matter Mater Phys.* 1997;56(15):9565-9574.
48. Willemen J "Modelling of amorphous silicon single- and multi-junction solar cells," Delft University of Technology, 1998.
49. Schenk A. Finite-temperature full random-phase approximation model of band gap narrowing for silicon device simulation. *J Appl Phys.* 1998;84(7):3684-3695.
50. Klaassen DBM. A unified mobility model for device simulation—I. Model equations and concentration dependence. *Solid State Electron.* Jul. 1992;35(7):953-959.
51. Altermatt PP, Schenk A, Geelhaar F, Heiser G. Reassessment of the intrinsic carrier density in crystalline silicon in view of band-gap narrowing. *J Appl Phys.* 2003;93(3):1598-1604.
52. Richter A, Werner F, Cuevas A, Schmidt J, Glunz SW. Improved parameterization of Auger recombination in silicon. *Energy Procedia.* 2012;27:88-94.
53. Shannon JM, Nieuwesteeg KJBM. Tunneling effective mass in hydrogenated amorphous silicon. *Appl Phys Lett.* 1993;62(15):1815-1817.
54. Synopsis, "Sentaurus device user," no. June. p. 2009, 2013.
55. Klein A, Körber C, Wachau A, et al. Transparent conducting oxides for photovoltaics: manipulation of fermi level, work function and energy band alignment. *Materials (Basel).* 2010;3(11):4892-4914.
56. Deane SC, Powell MJ. Defect chemical potential and the density of states in amorphous silicon. *Phys Rev Lett.* Mar. 1993;70(11):1654-1657.
57. Melskens J, Schouten M, Santbergen R, et al. In situ manipulation of the sub gap states in hydrogenated amorphous silicon monitored by advanced application of Fourier transform photocurrent spectroscopy. *Sol Energy Mater sol Cells.* 2014;129:70-81.
58. Kobayashi E, de Wolf S, Levrat J, et al. Increasing the efficiency of silicon heterojunction solar cells and modules by light soaking. *Sol Energy Mater Sol Cells.* 2017;173(June):43-49.
59. Tomasi A, Paviet-Salomon B, Jeangros Q, et al. Simple processing of back-contacted silicon heterojunction solar cells using selective-area crystalline growth. *Nat Energy.* Apr. 2017;2(5):17062. <https://doi.org/10.1038/nenergy.2017.62>
60. Kobayashi E, de Wolf S, Levrat J, et al. Light-induced performance increase of silicon heterojunction solar cells. *Appl Phys Lett.* Oct. 2016;109(15):153503. <https://doi.org/10.1063/1.4964835>
61. Bivour M, Temmler J, Steinkemper H, Hermle M. Molybdenum and tungsten oxide: high work function wide band gap contact materials for hole selective contacts of silicon solar cells. *Sol Energy Mater Sol Cells.* 2015;142:34-41.
62. Bivour M, Reichel C, Hermle M, Glunz SW. Improving the a-Si:H (p) rear emitter contact of n-type silicon solar cells. *Sol Energy Mater Sol Cells.* 2012;106:11-16.
63. Ritzau KU, Bivour M, Schröer S, et al. TCO work function related transport losses at the a-Si:H/TCO-contact in SHJ solar cells. *Sol Energy Mater Sol Cells.* 2014;131:9-13.

How to cite this article: Procel P, Xu H, Saez A, et al. The role of heterointerfaces and subgap energy states on transport mechanisms in silicon heterojunction solar cells. *Prog Photovolt Res Appl.* 2020;28:935-945. <https://doi.org/10.1002/pip.3300>